

Compact Robotically Steerable Image-Guided Instrument for Multi-Adjacent-Point (MAP) Targeting

Meysam Torabi, Rajiv Gupta, and Conor James Walsh, *Member, IEEE*

Abstract—Accurately targeting multi-adjacent points (MAPs) during image-guided percutaneous procedures is challenging due to needle deflection and misalignment. The associated errors can result in inadequate treatment of cancer in the case of prostate brachytherapy, or inaccurate diagnosis during biopsy, while repeated insertions increase procedure time, radiation dose, and complications. To address these challenges, we present an image-guided robotic system capable of MAP targeting of irregularly shaped volumes after a single insertion of a percutaneous instrument. The design of the compact CT-compatible drive mechanism is based on a nested screw and screw-spline combination that actuates a straight outer cannula and a curved inner stylet that can be repeatedly straightened when retracted inside the cannula. The stylet translation and cannula rotation/translation enable a 3-D workspace to be reached with the stylet's tip. A closed-form inverse kinematics and image-to-robot registration are implemented in an image-guided system including a point-and-click user interface. The complete system is successfully evaluated with a phantom under a Siemens Definition Flash CT scanner. We demonstrate that the system is capable of MAP targeting for a 2-D shape of the letter "H" and a 3-D helical pattern with an average targeting error of 2.41 mm. These results highlight the benefit and efficacy of the proposed robotic system in seed placement during image-guided brachytherapy.

Index Terms—Computer-assisted surgery, image-guided therapy, prostate intervention, steerable needles, surgical planning.

I. INTRODUCTION

SURGICAL needles are widely used for biopsy and treatment of cancerous tissues; however, because of mechani-

cal limitations, the needles have a narrow coverage zone and poor maneuverability even with lateral/vertical base manipulation [1], [2] and tissue manipulation [3].

Needle-based surgeries have advanced significantly in recent years with new technology developments in the areas of robotics and imaging. For visualization of the target tissue, X-ray computed tomography (CT) imaging provides high-contrast resolution with low noise as long as dense materials (e.g., metallic objects) are kept out of the imaging plane. CT-guided procedure workflows are desired to function with a minimal amount of imaging so as to minimize dosage for the patient. Compared with CT, magnetic resonance imaging (MRI) provides excellent tissue contrast and high resolution; however, the magnetic field imposes serious limitations and challenges in material selection and electromechanical design—in particular with actuators and electronics [4], [5].

Ultrasound (US) imaging is more accessible than CT and MRI, however, it produces lower quality images; it is also challenging to have continuous alignment of the needle within the imaging plane for its complete visualization during insertion [6].

One of the most prevalent needle-based procedures is image-guided brachytherapy, in which small radioactive seeds are deployed through a needle and permanently implanted into a tumor, as shown in Fig. 2. Likewise, prostate biopsy utilizes surgical needles to sample the selected regions of the prostate. Currently, both brachytherapy and biopsy are mainly performed free-hand, which limits the level of accuracy and reliability. The most common modality in prostate interventions is US imaging (e.g., [7], [8]), owing to its real-time nature; however, because of its poor resolution, the radioactive seeds are not well visualized in US images [4].

Typically, the targeting accuracy required for a given procedure depends on the specific clinical application. In high-dose rate brachytherapy in tandem and ovoid implantation procedures for patients with uterine or cervical cancer, high-level accuracy is required in order to ensure a uniform dose distribution. Targeting more deeply situated locations is more challenging than those close to the surface because small angular misalignments of the needle result in a large lateral displacement of its distal tip because of the need to pivot about a point at the skin surface. Furthermore, once inserted deep into the tissue, repositioning the distal tip of a straight percutaneous instrument is difficult, if not impossible, because of tissue-interaction forces along its length that resist its pivoting motion. Thus, if the needle is incorrectly placed, a radiologist is forced to retract it and attempt to reinsert it along the correct trajectory. This problem is exacerbated when

Manuscript received December 3, 2012; revised August 8, 2013 and December 15, 2013; accepted January 26, 2014. Date of publication March 20, 2014; date of current version August 4, 2014. This paper was recommended for publication by Editor F. Park upon evaluation of the reviewers' comments. This work was supported by the Wyss Institute for Biologically Inspired Engineering at Harvard University, the Deshpande Center for Technological Innovation at Massachusetts Institute of Technology, and the Department of Radiology at Massachusetts General Hospital.

M. Torabi was with the Harvard School of Engineering and Applied Sciences and Wyss Institute for Biologically Inspired Engineering, Harvard University, Boston, MA 02115 USA. He is now with the Harvard Medical School, Harvard University, Boston, MA 02115 USA (e-mail: torabi@bwh.harvard.edu).

R. Gupta is with the Department of Radiology, Massachusetts General Hospital, Harvard Medical School, Boston, MA 02114 USA (e-mail: rgupta1@partners.org).

C. J. Walsh is with the Harvard School of Engineering and Applied Sciences, Wyss Institute for Biologically Inspired Engineering, and Harvard Biodesign Lab, Harvard University, Cambridge, MA 02138 USA (e-mail: walsh@seas.harvard.edu).

This paper has supplementary downloadable material available at <http://ieeexplore.ieee.org>.

Color versions of one or more of the figures in this paper are available online at <http://ieeexplore.ieee.org>.

Digital Object Identifier 10.1109/TRO.2014.2304773

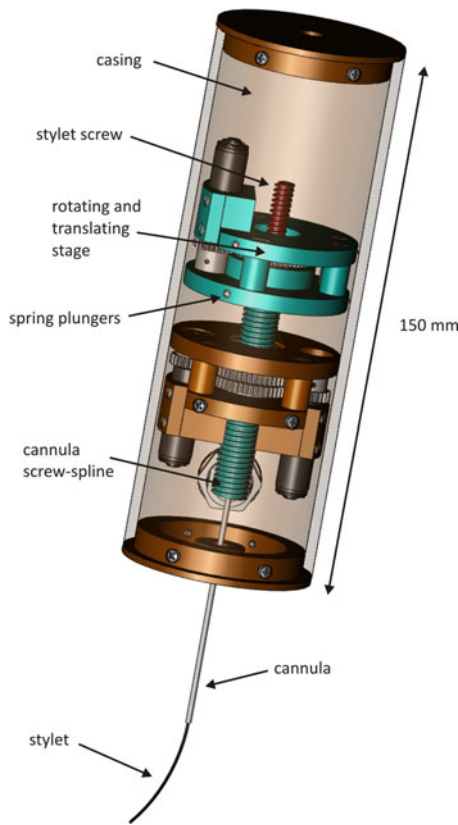


Fig. 1. Computer-aided drawing representation of the robotically steerable percutaneous instrument that can target multiple adjacent points in a volume in the soft tissue after a single needle insertion.

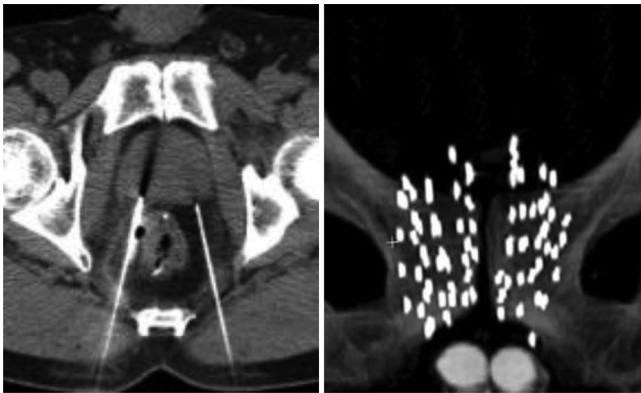


Fig. 2. CT-guided interventional procedures on the prostate. (Left) Two needles inserted bilaterally performing transgluteal prostate biopsy [11], [12]. (Right) Multi-adjacent seeds closely implanted within the prostate gland [13].

multiple adjacent points have to be targeted as in brachytherapy (see Fig. 2), because multiple needle insertions are typically required. One important consequence of these difficulties is that the procedures can become quite iterative and time-consuming and, therefore, require multiple scans, and an increased radiation dose and procedure time for the patient [9]. Therefore, there is a need for instruments that can accurately reposition the distal tip of an interventional tool to target multiple-adjacent points after a single needle insertion into the body.

Fig. 2 shows CT images that were acquired during interventional prostate procedures. The left figure shows two needles that

are placed in the prostate for biopsy, and the right one shows the distribution of multi-adjacent brachytherapy seeds inside the prostate. From the right figure, it can be seen that there is some randomness to the distribution of the seeds. Inaccuracy in seed delivery not only degrades the prostate cancer therapy but can also impose side effects such as erectile dysfunction, urinary retention, incontinence, and rectal injuries [10]. One may note that the accuracy in biopsy may be even more crucial than brachytherapy, since the radioactive seed placement is typically planned according to the biopsy results.

A. Prior Work

Over the past two decades, a number of medical robots have been developed in an attempt to improve needle placement in the soft tissue.

These robots are mounted on the CT scanner bed [14]–[16] or on the patient [17]–[19]. The majority of these manipulators provide a remote center of rotation so that the robot can pivot about the skin surface [20]–[23].

More recently, researchers have developed needle-steering robots to control the trajectory of the needle as it is inserted into the tissue. The two main strategies that have been employed to achieve higher maneuverability utilize asymmetric forces at the needle tip (e.g., due to bevel) [24]–[27] or rotation/translation of concentric precurved tubes [28]–[32].

The typical application for a bevel tip approach is when the needle must take a curved trajectory to avoid any obstacles and intersect targets along the way. A range of curved trajectories can be achieved by controlling the amount of time that the bevel spends in a particular orientation by rotating the needle in a spin-stop-spin-stop manner [25], [27]; however, bevel-tip-based approaches rely on a reaction force from the tissue to achieve steering; hence, steering is strongly dependent of the mechanical properties of the tissue, which is naturally inhomogeneous, and the needle. For prostate biopsy, it has previously been reported that the different layers of the tissue may limit the accuracy of needle placement due to nonuniform tissue stiffness [33]. For bevel-tip devices, the ability to steer and control the device is thus a function of both the geometry and material properties of the needle and tissue, and their interactions. Trajectory planning and target tracking algorithms have been developed and, as would be expected, have shown different behaviors in real and artificial tissues [34]. In the future, real-time imaging feedback may be used to improve controllability for these systems; however, the bevel orientation angle, which is the basis for steerability of this type of approach, cannot, at the moment, be measured. Therefore, alternative sensing is required to keep track of the needle-tip orientation.

An alternative to bevel-tip-based steering is to have a curve set into the distal tip of the needle to provide directionality to needle insertion [35], [36]. This approach has also been extended to applications using multiple concentric precurved tubes, which have the potential to increase control and accuracy because their planning is less dependent on tissue properties.

In 2006, Sears and Dupont [32], and Webster *et al.* [37] concurrently proposed this approach. The two groups also studied

the effect of external loads on the body of the tubes [31], [38]. Dupont *et al.* proposed a kinematic model that computed the resultant shape of an arbitrary number of tubes [39]. His group later modeled the frictional torque that is caused by the concentrated bending moments to improve the kinematic model [40] and presented closed-form inverse kinematics of the concentric tubes with constant curvatures [41]. Rucker and Webster improved the kinematics of the concentric tubes by accounting for torsional effects [42] and then extended the kinematic model to an unlimited number of tubes. They reported that the effect of torsion was required to determine active cannula bifurcation behavior and physical shape [28], which affects the targeting accuracy.

Another advantage of steerable needles is their multiple-target planning ability as mentioned in the literature [43]–[45]. Some recent experimental studies have evaluated the targeting accuracy of this concept, including Swaney *et al.* who evaluated the targeting accuracy of a concentric tube under 3-D US guidance [46], and Burgner *et al.* who tested a manually driven concentric tube using 2-D US [47]. Su *et al.* presented an MRI-compatible piezoelectrically actuated concentric tube [48], where they utilized an optical tracking system to evaluate the tip placement accuracy.

Much attention has been given to multi-degree-of-freedom bevel-tip-based and concentric precurved tube steering systems. They have been designed to navigate to arbitrary locations within the body through the use of large drive mechanisms that rotate and translate multiple concentric tubes. However, there has been less attention given to systems that have fewer degrees of freedom with more compact drive mechanisms. Webster *et al.* built a compact two degrees-of-freedom mechanism that could advance and rotate a needle better than an unaided human [49]. The needle was gripped between two rollers that drove needle advancement, and the rollers were rotated by a gear driven by a second motor. While simple and compact, this mechanism suffered from needle slippage in the traction drive and the authors felt that torque measurement would be necessary for accurate control. Salcudean *et al.* developed a compact mechanism that enabled active needle steering during insertion [29], [30] to correct for targeting errors. The device employed a stylet that was longer than the cannula so that up to 2 cm of the stylet's tip (which had a mild curve) could be selectively exposed. Two motors provided actuation; the steering direction was selected by rotating the stylet, and the steering rate was selected by controlling the amount that the stylet curve is exposed from the cannula.

When designing these compact lightweight systems that move curved stylets relative to straight cannulae, the requirements for the actuators are important so that they may be sized appropriately. Previous work by our team has experimentally measured the force as a function of various stylet and cannula geometries [50]; these data can be used to guide the design of compact drive mechanisms. Additionally, it would be beneficial to determine how differences in needle geometry and curvature affect certain aspects of the kinematics (e.g., exit angle) and stylet deflection in the tissue in order to select optimum system parameters for navigation.

In prostate interventions, inaccuracy in targeting stems from a variety of factors: a discrete area of insertion that is imposed by a rigid template with fixed hole spacing [10], needle deflection [33], tissue deformation [51], tissue motion during the intervention [52], [53], prostate swelling after the intervention [4], and poor visualization [52]. Currently, a template guide with an array of 169 holes is used, which is intended to guide parallel placement of needles with no angulation. Recently, Song *et al.* proposed a motorized template to specify the insertion position with improved resolution; however, insertion was performed manually [33].

B. Contribution

The robotic system that is presented in this paper uses a compact CT-compatible robust drive mechanism to steer a delivery needle that can deposit seeds through a hollow stylet in soft tissues. The robot specifications and proposed workflow were developed to be compatible with current prostate interventions. Mechanical design details of the robot were previously reported in [50], and [54]–[56], and in this paper, a closed-form inverse kinematics formulation is presented that models cannula deflection in addition to the clearance between the outer cannula and the inner stylet. An image-to-robot registration method is described that does not need an external registration frame but rather requires three pairs of feature points directly on the interventional tool. All of the aforementioned individual components were integrated and united into a custom image-guided-therapy (IGT) module in 3-D Slicer (National Alliance for Medical Image Computing, USA). Experimental trials for MAP targeting in a tissue-like environment were performed, demonstrating an average targeting error of 2.41 mm.

II. ROBOTICALLY STEERABLE INSTRUMENT

In this section, we present the mechanical design of the compact robotic tool, which is capable of repositioning the distal tip of a percutaneous instrument to reach multiple adjacent targets with a single insertion of the tool. The mechanism offers three degrees of freedom: translation of an inner stylet that has a precurved distal portion, and translation and rotation of a concentric outer cannula, which allows the stylet to be substantially straightened when retracted inside the cannula. A computer-aided drawing of this robotically steerable percutaneous instrument is shown in Fig. 1.

The first step in the design process was to determine the functional requirements, which was performed in collaboration with clinicians. The robot, while lightweight and CT-compatible, was required to provide a sufficient force to insert the cannula into the tissue by the three degrees of freedom with 1-mm translation and 1° angular accuracy. In order to address the sterility, the robot components were chosen to be low cost so that the entire device could potentially be disposable. Additionally, the minimum required targeting accuracy was determined to be 5.2 mm as this has been reported as the size of insignificant tumors in the prostate [57]. Furthermore, in another clinical study of prostate biopsy, the manual targeting accuracy was reported as 6.5 mm [58]. Hence, a robot device must demonstrate an

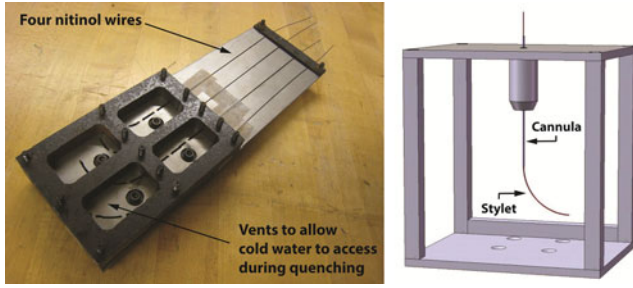


Fig. 3. (Left) Quench fixture with straight nitinol wire assembled. (Right) Test fixture for moving a stylet relative to a fixed cannula. It can be attached to an Instron machine and accepts a variety of cannula and stylet geometry.

improved accuracy compared with these values that are associated with manual interventions in order to be considered beneficial.

A. Stylet Design and Manufacture

The important dimensions pertaining to the design of the steering system are the stylet total bend angle, the stylet radius of curvature, and the diameters of the stylet and cannula. These dimensions determine the working volume that can be targeted, the necessary material constraints, the forces necessary to move the stylet relative to the cannula, and the stiffness of the stylet. Previously reported results of the force required for insertion into the soft tissue ranges from 2.3 to 15.6 N [59], [60] and depend on the size and type of needle used. In particular, it is worth mentioning that, in transperineal brachytherapy, the average force needed to navigate 17 and 18 G needles in the prostate was measured to be 6 and 5 N, respectively [60], which is within the aforementioned range. From simple beam bending mechanics, the longitudinal strain in the stylet was calculated for typical stylet and cannula geometry and it was determined that the stylet must be constructed from a superelastic material. A set of experiments was planned to determine the maximum force that is required to retract a curved nitinol stylet into a straight cannula. Using the fixture, 16 stylets with bend radii ranging from 10–40 mm and diameters of 0.508–0.990 mm were fabricated, and then tested with 14, 16, 18, and 20 gauge cannulas in the experimental setup that is described in [50]. A nitinol wire was obtained in a straight form (Forte Wayne Metals, Fort Wayne, IN, USA) and heat treatment was used to impart a curve into the distal end, using a previously reported method [14] that involved evenly heating the material to an annealing temperature of 550 °C and maintaining it at that temperature for 3 to 15 min until internal stresses have been relieved, which was followed by a quenching operation to preserve the material in the desired austenitic phase. The quench fixture, shown on the left in Fig. 3, was designed and built for this purpose, and provided the minimal thermal resistance to ensure rapid quenching.

The ranges for the deployment and retraction forces were found to be 0.2–7.0 and 0.3–14.0 N, respectively. In Fig. 3, on the right, the test fixture is shown, which was used to run the experiment to move the stylet relative to a cannula.

To understand the behavior of cannula and stylet insertion into the soft tissue, a number of bench level experiments were

TABLE I
MEAN TARGETING ERRORS FOR VARIOUS STYLET DIAMETERS AND RADII OF CURVATURE

Stylet Geometry	R = 10.85 [mm]	R = 21.55 [mm]	R = 31.72 [mm]
d = 0.635 [mm]	3.34 ± 0.77	1.61 ± 0.61	2.96 ± 2.16
d = 0.838 [mm]	3.26 ± 1.03	1.27 ± 0.72	2.47 ± 1.41

performed as described in [54]. In order to mimic real tissue, a phantom made from Vyse Ordnance Gelatin (Gelatin Innovations, Schiller Park, IL, USA) was utilized, since a properly calibrated 10% ordnance gelatin would reliably simulate the tissues [61]. It is worth mentioning that this type of gelatin has been recently used in the literature to develop a prostate phantom because of its similarity to the prostate tissue [62].

The experiments were performed for two different stylet diameters (i.e., 0.635 and 0.838 mm) and three different radii of curvature (i.e., 10.8, 21.5, and 31.72 mm). The positional information of the tip of the stylet was recorded and analyzed using MATLAB (Mathworks Inc., Natick, MA, USA).

This experiment was repeated a number of times for three different cannula axial positions and repeated with the cannula rotated 180°. Therefore, for each stylet, six data points were collected. The tip of the stylet was predicted using a series of homogeneous transformation matrices as described in [55]. A summary of the mean and standard deviations of the differences between the analytical and experimental data is shown in Table I.

Based on these results, it was determined that while some stylet deflection was observed, the amount was sufficiently small compared with our desired targeting accuracy discussed earlier. One interesting observation during the experiments was that as the cannula's tip translated downward, the cannula followed a slightly curved path in the tissue because of its slightly curved shape and resultant asymmetric forces on it. Thus, the targeting accuracy will be affected by both the deviation of the cannula because of tissue interaction forces, in addition to that of the stylet.

B. Mechanism Design

The mechanism design, constructed largely of plastic components for CT compatibility, is shown in Fig. 4. As mentioned, the device has a protruding cannula holding a preassembled stylet with a curved distal tip. The proximal end of the cannula is attached to the distal end of a hollow screw-spline, and the proximal end of the stylet is attached to the distal end of a screw, nested inside the screw-spline. Each attachment is achieved via aluminum-threaded inserts that are bonded to the proximal end of the shafts.

The screw-spline is a custom plastic ACME-threaded screw that also has a splined groove along its length. It is functionally similar to the ball-screw spline that is produced by THK (Schaumburg, IL, USA) that has been used in SCARA robots (e.g., EPSON RS3-Series, EPSON Robots, Carson, CA, USA) and other robotic applications in which the combination of translation and rotation are required in a compact design [63].

Fig. 4 shows nuts 1 and 2 engage the screw threads and spline, respectively. Nut 1 has a bore that is threaded to match

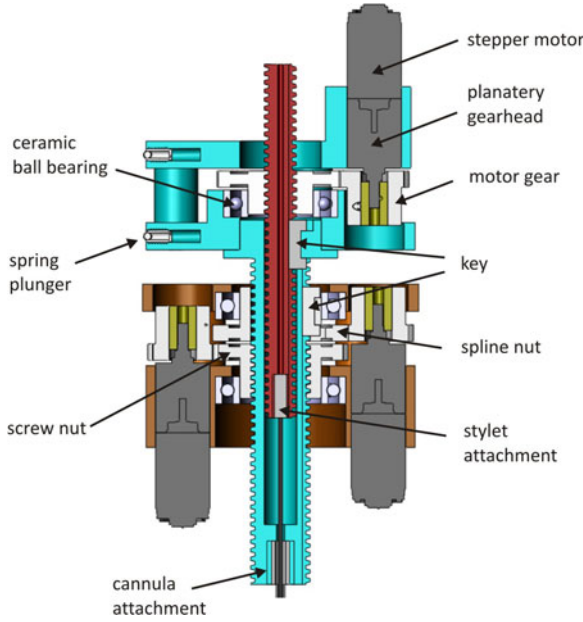





Fig. 4. Sectional view of the drive mechanism. A spline nut and screw nut engage the spline and threads of the screw-spline, respectively. Another threaded nut engages the screw that rides inside the screw-spline.

TABLE II
MODES OF OPERATION OF SCREW-SPLINE MECHANISM

Mode	Input		Cannula Movement	
	Screw Nut	Spline Nut	Translation	Rotation
	ω_1	0	$v = \omega_1 \frac{l}{2\pi}$	0
	$\omega_1 = \omega_2$	ω_2	0	ω_2
	0	ω_2	$v = \omega_2 \frac{l}{2\pi}$	ω_2

the lead of the screw, and nut 2 has a slot broached into the inside diameter that allows a small plastic 1.5-mm-wide key to be inserted. This key then engages the splined groove on the cannula screw-spline.

By appropriate control of the two nuts, three modes of operation of the screw-spline, and hence the cannula, with respect to the casing could be obtained as shown in Table II. The helix mode is not required for this application.

Translation of the stylet is achieved with the aid of a second ACME-threaded screw with a splined groove. A keyed feature on the inside of the screw-spline mates with the splined groove to constrain it from rotating with respect to the screw-spline, as shown in Fig. 4. The cannula screw-spline is capable of 360° of rotation, and the axial travel of both the cannula screw-spline and the stylet screw are 40 mm. The cannula's length is 13.5 cm to enable MAP targeting deep within the body, and the length of the stylet was selected so that it passes through the stylet screw and is accessible outside the casing. The stylet's base is hollow and attached to a cone-shape plastic container that can accommodate seeds. Fishing line can be used to push the seeds and release them from the stylet's tip into the medium. This

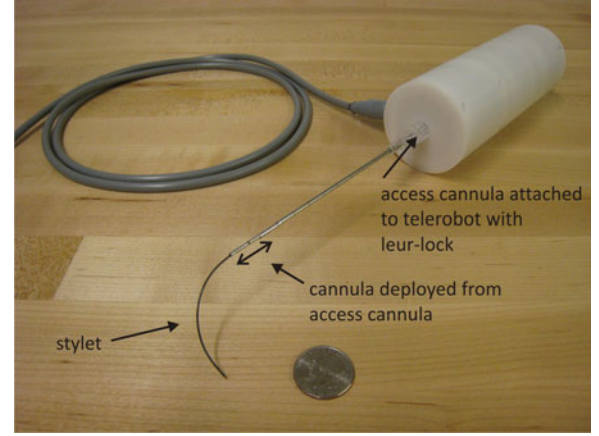


Fig. 5. Prototype of the robot. The stylet is shown in its deployed position. A quarter is shown for scale.

simple mechanism allowed an unlimited number of seeds to be deployed during the validation experiment.

A cylindrical precision ground tube (McMaster-Carr) housed all of the components. The system height and diameter were 15 and 5 cm, respectively, with a weight of approximately 180 g. An image of the prototype is shown in Fig. 5.

C. Mechanism Actuation and Transmission Selection

To simplify control, microstepper motors were chosen to actuate the nuts of the screw-spline and screw. As can be seen in Fig. 4, each of the nuts has an integral flange with spur gear teeth that mates with a spur gear attached to the gearhead shaft. Although not CT compatible themselves because of their metallic construction, two of the motors (for the screw-spline) are positioned so as to yield a metal-free scan plane. The third motor to actuate the stylet screw is also positioned away from the center of the device; however, depending on the rotational position of the screw-spline, it can occasionally show up in a CT image. Neglecting friction forces arising from bearings, the general equation to calculate the torque to raise a load and overcome frictional forces due to sliding contact between the threads is

$$T = \frac{F d_m}{2} \left(\frac{l + \pi \mu d_m \sec \alpha}{\pi d_m - \mu l \sec \alpha} \right) \quad (1)$$

where F is the desired maximum force, d_m is the pitch diameter of the lead screw, l is the lead, μ is the coefficient of friction between the threads, and α is the ACME thread angle (i.e., 29°).

Using a simple sliding test, the coefficient of the sliding friction of Acetal on Acetal was found to be 0.2. An ACME screw is not back drivable if the effective coefficient of thread friction is equal or greater than the tangent of the helix angle, i.e.,

$$\mu \geq \frac{l}{\pi d_m \sec \alpha}. \quad (2)$$

Thus, by choosing an appropriate lead and diameter for the screws, the cannula can retain its axial position when the stylet is being translated and vice versa.

A lead of 1/16 in (1.5875 mm) was chosen for the stylet screw and the cannula screw-spline. A stylet screw diameter

TABLE III
SUMMARY OF THE TRANSMISSION CHARACTERISTICS FOR THE CANNULA
SCREW-SPLINE AND STYLET SCREW IN ORDER TO ACHIEVE THE DESIRED
FORCES OF 15.6 AND 29.6 N, RESPECTIVELY

	Screw-Spline	Screw
Torque Required [Nmm]	23.9	28.1
Maximum Stress [MPa]	0.7	6.9
Efficiency [%]	15.9	26.6
Backdrivability	NO	NO

of 6 mm was chosen so that its bending stiffness would be sufficient for prototyping on a lathe. The screw-spline diameter was chosen to be 11 mm so that it just allowed the stylet screw to concentrically nest inside it. A summary of the results of the design calculations for the cannula screw-spline and stylet screw is shown in Table III. The table summarizes the transmission characteristics for the cannula screw-spline and stylet screw to achieve 15.6 and 29.6 N, respectively, where 15.6 N is the force that is needed to insert the cannula into the tissue, and 29.6 N is the total force to move the stylet relative to the cannula and insert the cannula into the tissue.

The stepper motors and gearheads that were selected for this application were of 10-mm diameter (AM1020, MicroMo Electronics, Faulhaber Group, Clearwater, FL, USA). The motors have a holding torque of 1.6 N·mm, and hence, a two-stage planetary gearhead with 16:1 reduction was chosen to meet the torque requirement. There was also a further gear reduction between the gearhead shaft and the nuts for the cannula screw-spline (2:1) and stylet screw (1.875:1). The stepper motors have a step angle of 18°, and therefore, this gear reduction also yields a minimum step angle for the screw-spline of just over half a degree (18/32), fulfilling the design specifications. The holding torque at the screw-spline nut was selected so as to constrain the screw-spline from rotating when desired.

The nuts for the screw and screw-spline were manufactured from off-the-shelf Acetal spur gears (SDP-SI, New Hyde Park, NY, USA); 24-mm-pitch diameter for the cannula screw-spline nut and 22.5-mm-pitch diameter for the stylet screw nut. Stainless steel spur gears with a pitch diameter of 12 mm (SDP-SI, New Hyde Park, NY, USA) were used to transmit the power from the planetary gearhead to the plastic spur-gear nuts.

III. KINEMATICS

The location of the instrument's tip inside the working volume depends on the relative position and orientation of the cannula and stylet whose interaction leads to various curvatures when penetrating the tissue. Since the degrees of freedom of the device consist of cannula translation (z_c), cannula rotation (θ_c), and stylet translation (z_s), the forward kinematics will establish a mapping between the input vector (θ_c, z_c, z_s) and the output vector as the location of the stylet's tip ($x_{tip}, y_{tip}, z_{tip}$), which ideally has overlap with the target or its vicinity. Once the orientation angle of the cannula θ_c is determined, the kinematics problem switches to a set of 2-D equations in a new YZ plane that has been rotated by θ_c about the Z-axis. The new YZ plane is where the two other parameters of the robot (z_c, z_s)

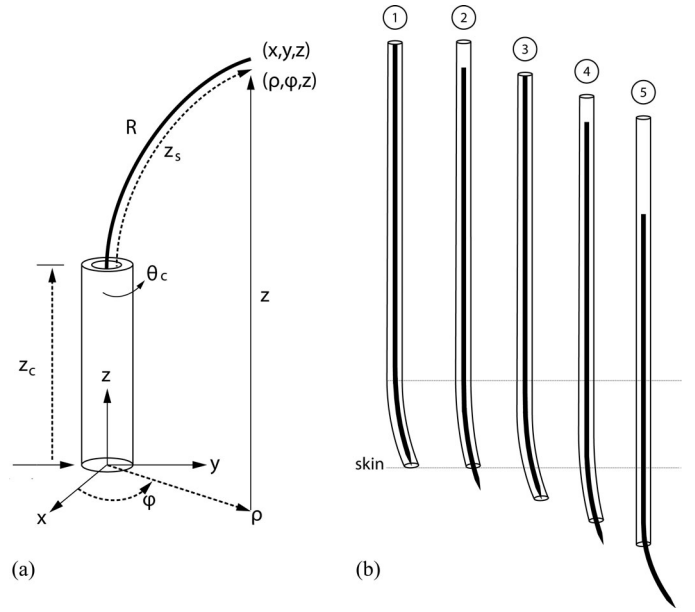


Fig. 6. (a) The cannula and stylet without the cannula deflection and the stylet exit angle, along with the associated parameters in the cylindrical coordinates. (b) Various relative positions of the cannula and stylet when penetrating tissue. While the curvature of the stylet is constant, the deflected part of the cannula demonstrates variable curvatures.

TABLE IV
PARAMETERS USED IN THE KINEMATICS FORMULATION

Definition	Name	Preset value
Total length of cannula [cm]	L_{total}	13.5
Cannula insertion [cm]	z_c	0.0
Maximum cannula insertion [cm]	z_c^{max}	4.0
Stylet insertion [cm]	z_s	0.0
Maximum stylet insertion [cm]	z_s^{max}	4.0
Stylet radius [cm]	R	5.6
Deflected-cannula radius [cm]	R_d	∞
Shared portion of cannula and stylet [cm]	L_0	z_s^{max}
Cannula rotation angle [rad]	θ_c	$-\pi \sim \pi$
Angular displacement of deflected cannula [rad]	θ_d	0.0
Angular displacement of stylet [rad]	θ_s	0.0
Minimum length of straight portion of cannula [cm]	z_{fixed}	$L_{total} - z_c^{max} \dots$ $\dots - z_s^{max}$

are investigated. This assumption is beneficial and helpful to simplify the modeling problem. In addition, the fact that there is no rotation/spinning inside the cannula, avoids any concern about synchronizing the tip and the base of the instrument either in torsional-compliance compensation or in lag-time reduction, as they have previously been shown to affect the formulation of the kinematics of such systems [64].

If the cannula is rigid relative to the stylet, and the cannula's inner diameter and the stylet's outer diameter are nearly equal, a straightforward formulation in cylindrical coordinates can represent the kinematics [see Fig. 6(a)], as presented in [55].

However, as shown in Fig. 6(b), while the curvature of the stylet is constant, the cannula will be deflected and its shape will be a function of the relative positions of the stylet and cannula. To account for this deflection and the stylet exit angle, a more realistic and accurate model was derived. The parameters that are used in the kinematics modeling are defined in Table IV.

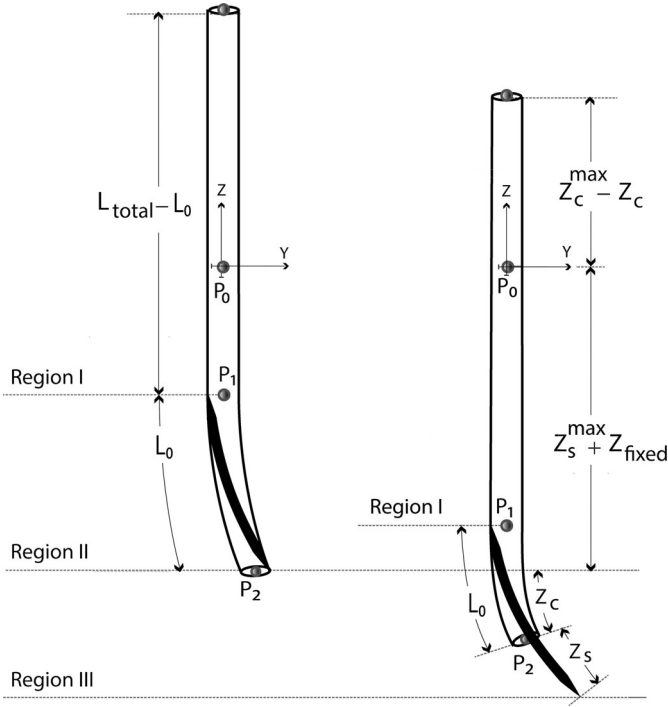


Fig. 7. Cannula and stylet before and after the insertion. The origin, the three nonoverlapping regions, the constant parameters, and the control variables, used in the kinematics formulation, have been shown.

A. Forward Kinematics

The modeling approach proposes the working YZ plane to be split into three nonoverlapping regions. The three regions and corresponding parameters that are assigned to each of them are shown in Fig. 7. The regions are classified based on the position of the cannula and stylet during the insertion task.

Region I is bounded from the bottom by the base of the curved portion of the stylet inside the cannula. The length of the total region changes during the insertion task and, as shown on the left in Fig. 7, it is equal to $L_{\text{total}} - L_0$.

Region II is bounded from above by region I and by the insertion point from below. Region III is defined as that part of the cannula–stylet that would be inside the body and is bounded from the bottom by the location of the stylet's tip.

The portion of the cannula that starts from the origin (i.e., P_0) and ends at P_1 (see Fig. 7) is always straight and never undergoes any deflection when the cannula has the stylet inside it. Since L_0 is the segment of the cannula, which can include the whole length of the stylet, it requires that $z_c^{\text{max}} \geq z_s^{\text{max}}$. When the stylet is retracted inside the cannula, the cannula is deflected, and the radius of this curvature is a function of material characteristics of the stylet and cannula as well as the radius of the stylet [37]. Defining R_d as the radius of the deflected cannula's curvature during the interaction of the cannula and stylet, the location of the cannula's tip, shown by P_2 in Fig. 7, relative to the origin will be

$$y_{P_2} = R_d (1 - \cos \theta_d) \quad (3)$$

$$z_{P_2} = -z_{\text{fixed}} - (z_s^{\text{max}} + z_c - L_0) - R_d \sin \theta_d \quad (4)$$

where $\theta_d = L_0/R_d$.

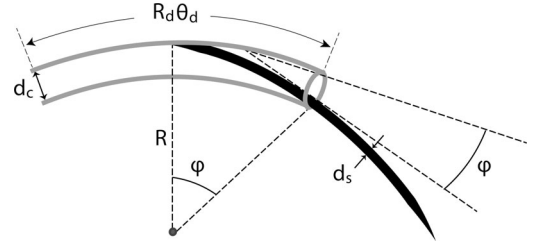


Fig. 8. Interaction of the deflected cannula and the curved stylet at the tip of the cannula causes an angle that directly affects the final location of the stylet's tip. While the cannula's curvature varies, φ is a constant angle.

It is worth mentioning that when the cannula starts to penetrate into the tissue, the stylet is entirely inside the cannula, and hence, the cannula has its maximum curvature; however, when the cannula translation and rotation are complete and the stylet is initially deployed from the cannula, the cannula will have a tendency to straighten, although the tissue may resist this somewhat.

As demonstrated in Fig. 8, the gap between the external body of the stylet and the internal body of the cannula prevents the stylet from exiting parallel to the tangent line of the cannula's tip, as mentioned in [65]. This angular difference is defined as φ in Fig. 8. By assuming that the stylet maintains its curvature before becoming tangent to the internal body of the cannula, the following expression for φ can be obtained:

$$\varphi = \frac{\pi}{2} - \sin^{-1} \left(1 - \frac{d_c - d_s}{R} \right). \quad (5)$$

This formulation implies that φ does not vary as a function of the relative position of the cannula and stylet. Furthermore, the aforementioned formula is consistent with the fact that if the internal diameter of the cannula is equal to the external diameter of the stylet, the stylet leaves the cannula tangential to the cannula's tip, and φ will be zero. Additionally, if $d_c < d_s$, which is physically impossible, the formula has an imaginary solution.

It can be shown that if φ was neglected, the amount of inaccuracy on the tip of the stylet would be calculated by

$$e_\varphi = 4R \sin \frac{z_s}{2R} \sin \left(\frac{\varphi}{2} \right) \quad (6)$$

which is computed for a case study in Section VI. Fig. 9(a), where φ is shown in yellow (darker area), shows that the absolute angle with which the stylet leaves the cannula is $\theta_d + \varphi$.

Therefore, the absolute angular displacement of the cannula and stylet will be $\theta_d + \varphi + \theta_s$, which is the approach angle of the stylet toward the target.

Finally, the absolute position of the tip of the stylet relative to the origin, $(y_{\text{StyleTip}}, z_{\text{StyleTip}})$, is obtained by

$$y_{\text{StyleTip}} = R_d (1 - \cos \theta_d) + R (\cos (\varphi + \theta_d) - \cos (\varphi + \theta_d + \theta_s)) \quad (7)$$

$$z_{\text{StyleTip}} = R (\sin (\varphi + \theta_d + \theta_s) - \sin (\varphi + \theta_d)) - z_{\text{fixed}} - (d_s^{\text{max}} - L_0 + z_c) - R_d \sin \theta_d. \quad (8)$$

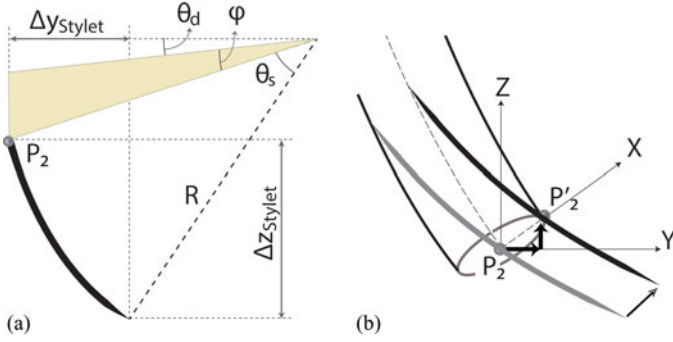


Fig. 9. (a) Angular and translational displacement of the stylet. (b) Clearance between the stylet and cannula needs to be considered in the kinematics in order to accurately predict the location of the tip. [(a) and (b) are shown in the same CS.]

To conclude Section III-A, one more factor needs to be added to the model. As shown in Fig. 9(b), while the location of P_2 is the center of the cross section of the cannula's tip, P'_2 is the actual exit point of the stylet. The stylet displacement between P_2 and P'_2 , which is projected on Y - and Z -axes, is

$$\Delta y = \frac{d_c - d_s}{2} \sin \theta_d, \quad \Delta z = \frac{d_c - d_s}{2} \cos \theta_d. \quad (9)$$

Due to the geometry of the problem, if this axial offset is neglected in the kinematics, the actual tip of the stylet will be thus offset by $\Delta x^2 + \Delta y^2$ from the cannula's tip. It is worth noting that this offset is a fixed value for a given cannula and stylet, while the error because of the cannula deflection depends on the overlap of the stylet and cannula as well as target depth, and consequently is a function of the target location.

The final answer will be obtained by rotating y_{styleTip} and z_{styleTip} , which is formulated in (7) and (8), by $-\theta_c$ around the Z -axis back to the original YZ plane.

B. Inverse Kinematics

In order to position the tip of the stylet within the tissue toward a desired target, an inverse kinematic model is required. Starting from the forward kinematics formulated earlier in (7) and (8), and rearranging it, the following equations are obtained:

$$\frac{y_{\text{target}}}{R} - \frac{R_d}{R} + \cos \gamma = \frac{-R_d}{R} \cos \theta_d + \cos(\theta_d + \varphi) \quad (10)$$

$$\frac{z_{\text{target}}}{R} + \frac{D}{R} + \sin \gamma = \frac{-R_d}{R} \sin \theta_d + \sin(\theta_d + \varphi) \quad (11)$$

where R and R_d are radii of the stylet and the deflected cannula, respectively, and γ and D are defined as

$$\gamma = \varphi + \theta_d + \frac{(z_s^{\text{Max}} - R_d \theta_d)}{R}, \quad D = z_{\text{fixed}} + z_s^{\text{Max}} - L_0 + z_c. \quad (12)$$

For the purpose of obtaining the closed-form formula for the stylet insertion length, namely z_s , (10) can be rewritten as

$$\left(\frac{R_d}{R} - 1 \right) \frac{\theta_d^2}{2} - \varphi \theta_d + \left(1 - \frac{\varphi^2}{2} - \frac{y_{\text{target}}}{R} - \cos \gamma \right) = 0 \quad (13)$$

which appears to be a second-order equation of θ_d ; however, the coefficients are not all constant and are a function of θ_d . However, it will be shown that an accurate approximation of (13) can help derive a closed-form solution for z_c and z_s . The validity of this approximation is later validated using various geometries of the stylet and cannula. Equation (13), after the approximation, is then

$$(a - Rn^2) \theta_d^2 + (b - 2Rmn) \theta_d + (2R - Rm^2 + k) = 0 \quad (14)$$

where a , b , m , n , and k are

$$a = R - R_d, \quad b = 2R\varphi, \quad m = \varphi + z_s^{\text{Max}}/R, \quad n = 1 - R_d/R, \quad k = -2R + R\varphi^2 + 2y_{\text{target}}. \quad (15)$$

Therefore, the solution for the stylet insertion length is

$$z_s = z_s^{\text{Max}} - R_d \frac{\sqrt{(\theta_d - mn)^2 - (a/R - n^2)} - (2 - m^2/R)}{(a/R - n^2)} \quad (16)$$

which is a real, positive, and *unique* solution, if the target is located inside the feasible area.

The equation (16) shows that z_s does not depend on the vertical location of the target, which is consistent with the simple model that is presented in [55].

Finally, using (11), z_c is calculated by the following nonlinear exact formulation:

$$z_c = -z_{\text{target}} + R \sin(\varphi + \theta_d) - R \sin(\varphi + \theta_d + z_s/R) - R_d \sin \varphi. \quad (17)$$

Before performing an experimental test of the system, the kinematics formulation was evaluated by discretizing the feasible area and running simulation tests recursively for all possible targets. The inverse kinematics routine in the simulation attempted to reach to every single feasible target and computed the input vector (θ_c, z_c, z_s) . This vector was then used to compute the location of the stylet's tip, $(x_{\text{tip}}, y_{\text{tip}}, z_{\text{tip}})$, and the Euclidean difference between this and the original target was calculated. This simulation was run for different geometries using various inner diameters for the cannula: 1.2, 1.6, 2.0, and 2.4 mm, and various outer diameters for the stylet: 0.5, 0.7, 0.9, and 1.1 mm using the stylet's radii of 35, 45, 50, and 55 mm. For all combinations, the error distribution demonstrated a mean of consistently less than 0.60 mm with a variance of 0.51 mm.

Finally, the inverse kinematics formulated in this section requires an image-to-robot registration. The following section explains how the registration adapts the inverse kinematics for any arbitrary relative position and orientation of the robot and the CT scanner.

IV. IMAGE-TO-ROBOT REGISTRATION

Using a set of feature points on the robot that can be identified in medical images, the *orientation*, *position*, and *scaling* of the robot coordinate system (CS) relative to the image CS in 3-D can be calculated. We developed a point-based registration that mathematically requires at least three pairs of spatial points

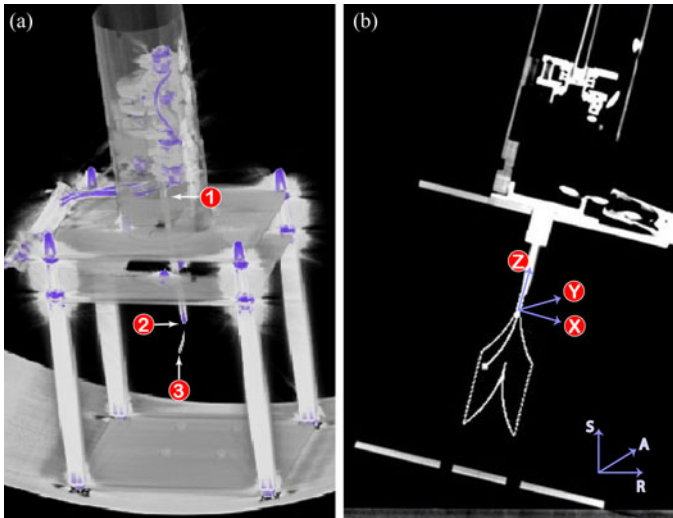


Fig. 10. (a) Three-dimensional-reconstructed image from 2-D CT slices. The location of the three registration points on the cannula and stylet are pointed. (b) Robot is intentionally inclined with respect to the scanner CS, and the registration has adapted the feasible area, the path, and the target to execute the inverse kinematics along the correct geometry.

which were chosen on the base of the cannula, the tip of the cannula, and the tip of the stylet, as shown in Fig. 10(a).

Since the registration points are considered on the needle instead of an external frame (such as that proposed in [66]), the procedure registers the image to the needle, not to the robot, thus eliminating potential errors between the drive mechanism, cannula, and stylet. In this regard, after the preprocedural imaging, the user clicks on the screen to specify the location of the registration points as well as the insertion point. Fig. 10(b) demonstrates how the target, the feasible area, and the planned path can then be superimposed over the CT images after the registration.

V. NAVIGATION SOFTWARE DESIGN

A new image-guided therapy module was designed and developed for the robot. The module was initiated, in part, from the ProstateNav module (Brigham and Women's Hospital, Boston, MA, USA) [67] whose workflow was clinically inspired from image-guided prostate interventions. In this section, we explain our proposed system architecture.

The procedure starts with an initial configuration, which includes importing the robot parameters to the module, preparing the network connection, and setting up the communication between the navigation software (3-D Slicer [68]) and the external software (Galil library) via OpenIGTLink [69].

Following this, the preprocedural imaging step starts by placing the robot inside the CT bore on the intervention bed, deploying the entire stylet, scanning the robot, and loading the DICOM files into 3-D Slicer for the purpose of registration.

The user clicks on the desired target or targets and if they are confirmed by the module as reachable, then the inverse kinematics is computed, and the registered needle-path is superimposed on the medical images. The module allows the user to localize up to 100 targets per cannula-insertion by consecutively click-

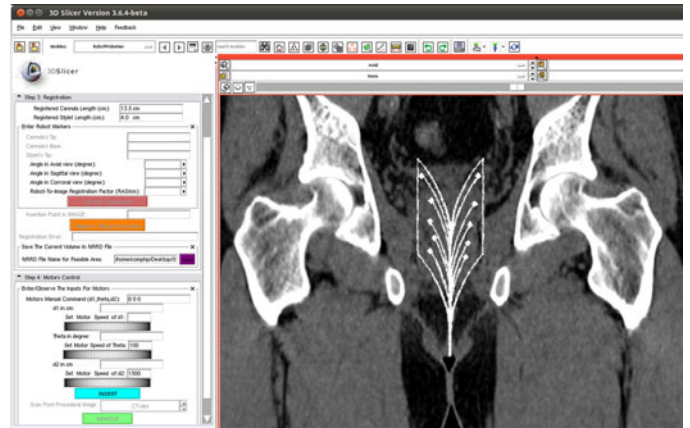


Fig. 11. Registered 3-D feasible volume is aligned on the prostate image demonstrating a transperineal prostate therapy case. The multiple paths are visualized using inverse kinematics. The left side shows part of the widgets designed in 3-D Slicer for importing the needle specifications, the registration parameters, and the motor commands. The CT image is taken from [72].

ing on the points of interest in the medical image that are then recorded by the software. As a result, with two insertions, up to 200 seeds can be placed within the accessible zone. This is clinically important as in the low-dose rate brachytherapy protocol, 50–150 seeds are deposited within the prostate [70].

As shown in Fig. 11, the feasible zone can sit in the region of interest so that the stylet has sufficient maneuverability and access within the prostate. This is a typical scenario of transperineal prostate therapy [71]. Note that the manual operation of this procedure requires multiple insertions, while steerability of the stylet and cannula would obviate the need for multiple insertions of conventional straight needles.

With this procedure workflow, the physician is always in the loop and is able to cancel or modify the procedure if needed.

The interface workflow was such that after the three parameters, θ_c , z_c , and z_s were computed, they were converted to the corresponding number of steps according to the design of the gearbox between the stepper motor's shaft and the screw-spline. Then, the commands were sent to the motor controller upon approval from the physician. For multiple-target planning, targets were resorted to minimize the total rotation of the cannula. In this way, regardless of the number of targets, the total rotation of the cannula never exceeded 360° , which resulted in minimal angular backlash.

After reaching a target and retracting the stylet back to the home position, the cannula axial position could be adjusted for the next target and then rotated so as to place the stylet in the correct orientation. Once the stylet reached the intended location, a small seed was released from the tip and deposited into real or artificial tissue. The time from when the user clicked on the medical image to when a seed was deposited was found to be on average 45 s, shorter than the time typically required for manual operations. After the interventional task, the robot moved inside the bore for imaging, and the pre- and postprocedural images could be overlaid so that the user could visually compare the planned and actual paths.

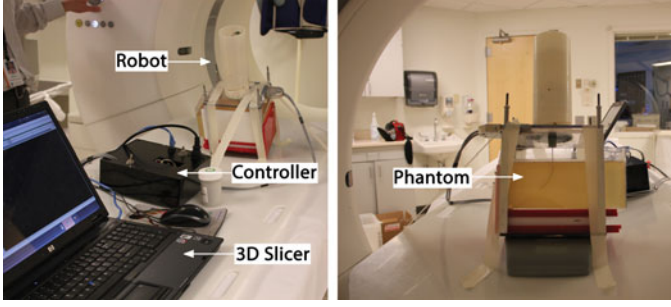


Fig. 12. Robot, positioned with some arbitrary angles on the CT scanner bed, ready to move inside the bore for preprocedural imaging. A laptop computer was connected via the Ethernet to 3-D Slicer where the graphical user interface, the robot kinematics, and the registration were developed and integrated into the new IGT module.

All the information, including the target position, the stylet's tip position, the three registration points, the inverse kinematics parameters, and the registration parameters were saved in a file and kept with the pre- and postprocedural images to facilitate offline analysis of the data.

VI. EXPERIMENTAL RESULTS

We demonstrated four different patterns of deployed seeds using the concept of MAP targeting, and two of these were analyzed quantitatively using a CT imaging system at Massachusetts General Hospital. A Dual Source MDCT scanner (Definition Flash, Siemens Medical Solutions, Erlangen, Germany) was used for scanning at 120 kV, 200 mA, pitch of 1, 0.6-mm slice thickness, and approximately 0.4-mm in-plane resolution. The image data, therefore, have a localization accuracy of approximately 0.4 mm in the XY plane, and approximately 0.6 mm in the Z -direction.

Two photographs of the experimental setup are shown in Fig. 12. As explained in Section II, we used a 10% ordnance gelatin phantom to mimic the real tissue [61]. The phantom was mounted within the apparatus made from aluminum and was tightly fixed to the scanner bed. The robot was seated at a preset height on top of the apparatus so that the cannula's tip touched the phantom's surface. A CT image of the apparatus is shown in Fig. 10.

A curved hollow stylet with 35.5 mm radius and length of 40 mm was used along with a 135 mm length cannula, 40 mm of which could be navigated within the gelatin by the steering mechanism. The size of the feasible volume accessible for the aforementioned cannula and stylet was calculated with the following formula:

$$V_{\text{zone}} = \pi z_c^{\text{max}} R^2 \left(1 - \cos \frac{z_s^{\text{max}}}{R} \right)^2 \quad (18)$$

which, for the geometry selected, was 51.53 cm^3 . This was a small zone ($\sim 3\%$) of the 1800-cm^3 volume of the entire box of gelatin. Note that the average size of a swollen prostate is estimated to be 45 cm^3 [73], and thus, the selected stylet and cannula would be suitable for prostate interventional procedures. Considering the feasible zone as a cylinder, the diameter

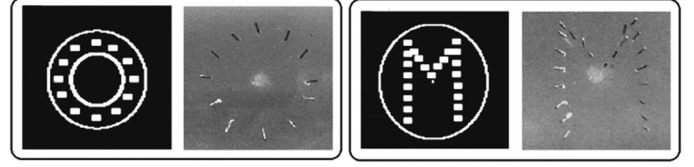


Fig. 13. Planned and the actual patterns of the letters “O” and “M” with 12 and 23 multi-adjacent targets, respectively, shaped in the gelatin by the deposition of the seeds. The brighter small zone in the center of the gelatin shows the vertical path of the cannula.

of this cylinder is

$$d_{\text{zone}} = 2r \left(1 - \cos \frac{z_s}{R} \right)^2 \quad (19)$$

which, in the case of the selected stylet, could be up to 40 mm. Since the average size of the prostate in the lateral direction and the anterior–posterior direction is 50 and 35 mm, respectively [4], it is possible to reach 80% of the lateral cross section and 100% of the anterior–posterior cross section of a typical prostate when the selected stylet is entirely deployed. It should be noted that tumors are typically noticeably smaller than the entire prostate.

The cannula's internal and external diameters were 1.90 and 2.10 mm, respectively, while the stylet's internal and external diameters were 0.90 and 1.20 mm respectively. According to (5), this cannula–stylet geometry resulted in 11.4° for the stylet exit deviation angle from the cannula. This angle, as mentioned in Section III, would create the following potential maximum error at the tip of the stylet:

$$e_\varphi = 4R \sin \frac{z_s}{2R} \sin \left(\frac{\varphi}{2} \right) = 7.6 \text{ mm} \quad (20)$$

which is significant for typical interventional procedures.

Initial results of seed deployment experiments with the integrated system were consistently acceptable as shown by the strong similarity between the specified pattern and that produced. Two examples are presented in Fig. 13 demonstrating that the robot is capable of creating complex patterns of seeds. The robot's capability of placing the radioactive seeds with specific patterns within the tissue is necessary to optimize the radiation dose for effective treatment of prostate cancer [4] while ensuring a safe dose for healthy tissues [74]. In the CT images, the cannula and stylet were clearly visible with minimal artifacts, as shown in Fig. 10(b). It is also apparent from the figure that the motors are all out of the scan plane.

In order to quantitatively assess the targeting accuracy of the system, the robot was commanded to reach 13 targets that are arranged in the shape of the letter “H.” For these experiments (setup shown in Fig. 12), the robot's casing had arbitrary angles with the axes of the image CS so as to validate the registration. The robot was commanded to create a 2-D seed deployment pattern to demonstrate that the concept of MAP targeting could be applied to a *thin* layer in surgical sites.

The result, captured from the CT images, is plotted in Fig. 14 depicting the letter “H.” Note that the size of each target was a voxel size, and the size of the seeds was 3 mm similar to that of actual radioactive seeds. The robot was not reinitialized during

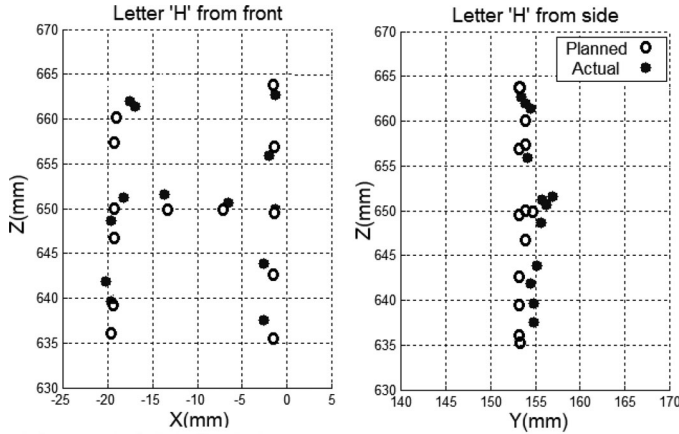


Fig. 14. Data points for letter “H” are captured from the CT-images from the front and side. The targeting errors were distributed over the 13 targets by the mean and the standard deviation of 2.53 and 1.00 mm, respectively.

TABLE V
PARAMETERS USED/CALCULATED FOR CREATING “H” AND HELIX

Parameter definition	Value (Letter H)	Value (Helix)
Number of consecutive targets	13	8
Inserted stylet length range [cm]	0.72 ~ 2.72	2.62 ~ 3.30
Inserted cannula length range [cm]	0.99 ~ 3.26	2.56 ~ 3.92
Targeting accuracy's mean [mm]	2.53	2.30
Targeting accuracy's standard deviation [mm]	1.00	1.00
Maximum targeting error [mm]	4.63	3.84
Minimum targeting error [mm]	0.93	1.18
Registration angles in RAS CS [deg]	(161.5, 25.1, 180)	(180, 0, 165)
Stylet translation velocity [mm/s]	2.30	2.30
Cannula translation velocity [mm/s]	3.10	3.10
Cannula rotation velocity [rad/s]	1.30	1.30

the sequential targeting, and it was observed that the error did not appear to increase throughout the course of the experiment. In evaluating the system, we note that the overall targeting accuracy is a function of the accuracy of the mechanical system, the kinematics formulation, the image-to-robot registration, and any deflection of the cannula and stylet because of the interaction forces with the tissue. As reported in Table V, this flat shape required the robot to generate various lengths in z_s and z_c , and the targeting error had a mean and standard deviation of 2.53 and 1.00 mm, respectively. The error in the y -direction ranged from 0.10 to 2.43 mm with a mean of 1.32 mm and the standard deviation of 0.73 mm, indicating that the layer of seeds created an approximate 2-D plane in gelatin.

The second experiment was to create a helical pattern with eight seed deployments. As in the first experiment for the H shape, the robot was placed within the scanner in an arbitrary configuration to ensure that both translational and rotational aspects of the registration could be evaluated. The maximum and minimum values of the targeting errors were 3.84 and 1.18 mm, respectively (see Table V). The mean error (2.30 mm) and standard deviation (1.00 mm) were very similar to those for the H shape experiment. Fig. 15 shows the results of “H” and helix inside the working zone, as captured by the CT images.

Improvements to the registration algorithm could be achieved by adopting automatic segmentation approaches to remove the variability of the current manual approach. Furthermore, a better

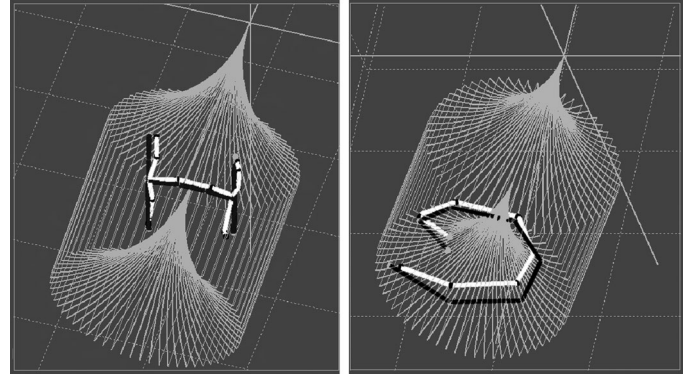


Fig. 15. Black and white plots, visualized inside the feasible volume, are the planned and actual shapes, respectively. The letter “H” with 13 targets and helix with eight targets are consecutively reached in the gelatin. The overall error average for all 21 targets was limited to the mean of 2.41 ± 1.00 mm (standard deviation). The data were imported from CT-images.

understanding of how the deflection of the cannula and stylet is influenced by the tissue as in [75] may also lead to an improved ability to determine the actuator inputs to achieve a desired stylet's tip position. We have included supplementary video file that demonstrates both the drive mechanism and the ability of the robot to reposition the distal tip of the stylet to reach multiple adjacent targets and deposit the seeds at the preplanned locations in the gelatin.

VII. CONCLUSION

We have shown that the proposed computer-integrated medical robotic system, including the hardware and software, is capable of accurate MAP targeting in a phantom model.

The proposed architecture integrates with the current clinical workflow through a set of sequential operations that include: initial configuration, preprocedural imaging, robot registration, MAP targeting planning, robot actuation, seed deployment, and follow-up postprocedural imaging.

We derived closed-form inverse kinematics, implemented a new point-based registration, designed the navigation software, and evaluated the full image-guided robotic system in a clinical setting. Our results exhibited a 2.41-mm average targeting error for multiple consecutive, adjacent targets, with no feedback indicating a high-level performance of the overall system compared to the current manual approach. The 2-D and 3-D MAP targeting we present were achieved with only a preprocedural planning and final confirmation CT-scan, demonstrating the potential for the reduction of the required number of CT scans.

We demonstrated that the navigation software and the targeting accuracy results are also in line with prostate interventional procedures. The worst targeting error was 4.63 mm, which is below the threshold defined in the design requirements of the robot. The error threshold was based on the size of insignificant tumors in the prostate, which is equal to that of a sphere with a radius of 5.2 mm or less [57].

An assumption of our approach is that a single set of planning images are sufficient for MAP targeting. This is based on the

fact that the motion of the prostate during the intervention is significantly less than that of other organs because of its distal location and support from the pelvic structure [57]. As the next immediate step, this assumption needs to be validated in animal or clinical studies, and if necessary, planning algorithms that account for any potential tissue deformation could be incorporated into the system.

From a clinical perspective, the robotic mechanism, while CT-compatible, is sufficiently lightweight and compact such that it could be patient-mounted or attached to the end-effector of a gross passive positioning system [76]. The sterility was also addressed by making the entire device low cost and potentially disposable.

These results show that the proposed image-guided system can create accurate conformal maps within the tissue and has the clinical potential to reduce the number of needle insertions, associated radiation dose, and procedure time.

ACKNOWLEDGMENT

The authors would like to thank Prof. A. Slocum at MIT for his input in the initial mechanical design.

REFERENCES

- [1] S. P. DiMaio and S. E. Salcudean, "Needle steering and motion planning in soft tissues," *IEEE Trans. Biomed. Eng.*, vol. 52, no. 6, pp. 965–974, Jun. 2005.
- [2] N. J. Cowan, K. Goldberg, G. S. Chirikjian, G. Fichtinger, R. Alterovitz, K. B. Reed, V. Kallem, W. Park, S. Misra, and A. M. Okamura, "Robotic needle steering: Design, modeling, planning, and image guidance," in *Surgical Robotics—Systems, Applications, and Visions*, J. Rosen, B. Hannaford, and R. Satava, Eds. New York, NY, USA: Springer, 2011, pp. 557–582.
- [3] M. Torabi, K. Hauser, R. Alterovitz, V. Duindam, and K. Goldberg, "Guiding medical needles using single-point tissue manipulation," in *Proc. IEEE Int. Conf. Robot. Autom.*, May 2009, pp. 2705–2710.
- [4] G. S. Fischer, I. Iordachita, C. Csoma, J. Tokuda, S. P. DiMaio, C. M. Tempny, N. Hata, and G. Fichtinger, "MRI-compatible pneumatic robot for transperineal prostate needle placement," *IEEE/ASME Trans. Mechatronics*, vol. 13, no. 3, pp. 295–305, Jun. 2008.
- [5] F. Wu, M. Torabi, A. Yamada, A. Golden, G. Fischer, K. Tuncali, D. Frey, and C. Walsh, "An MRI coil-mounted multi-probe robotic positioner for cryoablation," presented at the ASME Int. Design Eng. Tech. Conf. Comput. Inform. Eng. Conf., Portland, OR, USA, Aug. 2013.
- [6] L. J. Brattain, C. Floryan, O. P. Hauser, M. Nguyen, R. J. Yong, S. B. Kesner, S. B. Corn, and C. J. Walsh, "Simple and effective ultrasound needle guidance system," in *Proc. IEEE Int. Conf. Eng. Med. Biol. Soc.*, Aug. 2011, pp. 8090–8093.
- [7] G. Fichtinger, E. C. Burdette, A. Tanacs, A. Patriciu, D. Mazilu, L. L. Whitcomb, and D. Stoianovici, "Robotically assisted prostate brachytherapy with transrectal ultrasound guidance—Phantom experiments," *Brachytherapy*, vol. 5, pp. 14–26, Jan./Mar. 2006.
- [8] Y. Yu, T. K. Podder, Y. Zhang, W-S. Ng, V. Misic, J. Sherman, L. Fu, D. Fuller, E. Messing, D. J. Rubens, J. G. Strang, and R. Brasacchio, "Robot-assisted prostate brachytherapy," in *Proc. Med. Image Comput. Comput.-Assisted Intervention*, 2006, pp. 41–49.
- [9] C. J. Walsh, B. H. Sapkota, M. K. Kalra, N. C. Hanumara, B. Liu, J. A. Shepard, and R. Gupta, "Smaller and deeper lesions increase the number of acquired scan series in computed tomography-guided lung biopsy," *J. Thorac. Imag.*, vol. 26, no. 3, pp. 196–203, Aug. 2011.
- [10] S. E. Salcudean, T. D. Prananta, W. J. Morris, and I. Spadinger, "A robotic needle guide for prostate brachytherapy," in *Proc. IEEE Int. Conf. Robot. Autom.*, Pasadena, CA, USA, May 2008, pp. 2975–2981.
- [11] D. A. Gervais, *Interventional Radiology Procedures in Biopsy and Drainage*. New York, NY, USA: Springer, 2011.
- [12] D. J. Krauss, K. G. Clark, I. S. Nsouli, R. M. Amin, C. M. Kelly, and M. A. Mortek, "Prostate biopsy in patients after proctectomy," *J. Urol.*, vol. 149, no. 3, pp. 604–606, Mar. 1993.
- [13] S. Daniel, C. Rabbani, A. Aref, R. Taylor, D. Patel, and P. J. Chuba, "Three-dimensional visualization and dosimetry of stranded source migration following prostate seed implant," *J. Practical Radiation Oncol.*, vol. 2, no. 3, pp. 193–200, Jul./Sep. 2012.
- [14] A. Bzostek, A. C. Barnes, R. Kumar, J. H. Anderson, and R. H. Taylor, "A testbed system for robotically assisted percutaneous pattern therapy," in *Proc. Med. Image Comput. Comput.-Assisted Intervention*, 1999, pp. 1098–1107.
- [15] D. Stoianovici, K. Cleary, A. Patriciu, D. Mazilu, A. Stanimir, N. Craciunoiu, V. Watson, and L. Kavoussi, "AcuBot: A robot for radiological interventions," *IEEE Trans. Robot.*, vol. 19, no. 5, pp. 927–930, Oct. 2003.
- [16] M. Rasmus, S. Dziergwa, T. Haas, P. Madoerin, R. Huegli, D. Bilecen, and A. L. Jacob, "Preliminary clinical results with the MRI-compatible guiding system INNOMOTION," *Int. J. Comput. Assisted Radiol. Surg.*, vol. 2, pp. S138–S145, 2007.
- [17] E. Taillant, J.-C. Avila-Vilchis, C. Allegrini, I. Bricault, and P. Cinquin, "CT and MR compatible light puncture robot: Architectural design and first experiments," in *Proc. Med. Image Comput. Comput.-Assisted Intervention*, 2004, pp. 145–152.
- [18] B. Maurin, B. Bayle, J. Gangloff, P. Zanne, M. de Mathelin, and O. Piccin, "A robotized positioning platform guided by computed tomography: Practical issues and evaluation," in *Proc. IEEE Int. Conf. Robot. Autom.*, 2006, pp. 251–256.
- [19] C. Walsh, N. Hanumara, A. Slocum, J.-A. Shepard, and R. Gupta, "A patient-mounted, telerobotic tool for CT-guided percutaneous interventions," *ASME J. Med. Devices*, vol. 2, pp. 011007-1–011007-10, Mar. 2008.
- [20] R. H. Taylor, J. Funda, B. Eldridge, S. Gomory, K. Gruben, D. LaRose, M. Talamini, L. Kavoussi, and J. Anderson, "A telerobotic assistant for laparoscopic surgery," in *Proc. IEEE Int. Conf. Eng. Med. Biol. Soc.*, 1995, pp. 279–288.
- [21] N. Hata, R. Hashimoto, J. Tokuda, and S. A. M. S. Morikawa, "Needle guiding robot for MR-guided microwave thermotherapy of liver tumor using motorized remote-center-of-motion constraint," in *Proc. IEEE Int. Conf. Robot. Autom.*, 2005, pp. 1652–1656.
- [22] E. Bocktor, R. J. Webster, H. Mathieu, A. Okamura, and G. Fichtinger, "Virtual remote center of motion control for needle placement robots," *Comput. Aided Surg.*, vol. 9, pp. 175–183, 2004.
- [23] S. E. Song, J. Tokuda, K. Tuncali, A. Yamada, M. Torabi, and N. Hata, "Design evaluation of a double ring RCM mechanism for robotic needle guidance in MRI-guided liver interventions," in *Proc. IEEE/RSJ Int. Conf. Intell. Robot. Syst.*, Nov. 2013, pp. 4078–4083.
- [24] R. J. Webster, III, J. S. Kim, N. J. Cowan, G. S. Chirikjian, and A. M. Okamura, "Nonholonomic modeling of needle steering," *Int. J. Robot. Res.*, vol. 25, no. 5–6, pp. 509–525, May/Jun. 2006.
- [25] J. A. Engh, G. Podnar, S. Y. Khoo, and C. N. Riviere, "Flexible needle steering system for percutaneous access to deep zones of the brain," in *Proc. IEEE 32nd Northeast Bioeng. Conf.*, 2006, pp. 103–104.
- [26] K. B. Reed, A. Majewicz, V. Kallem, R. Alterovitz, K. Goldberg, N. J. Cowan, and A. M. Okamura, "Robot-assisted needle steering," *IEEE Robot. Autom. Mag.*, vol. 18, no. 4, pp. 35–46, Dec. 2011.
- [27] J. Engh, D. Minhas, D. Kondziolka, and C. Riviere, "Percutaneous intracerebral navigation by duty-cycled spinning of flexible bevel-tipped needle," *Neurosurgery*, vol. 67, no. 4, pp. 1117–1122, 2010.
- [28] R. J. Webster, III, J. M. Romano, and N. J. Cowan, "Mechanics of precurved-tube continuum robots," *IEEE Trans. Robot.*, vol. 25, no. 1, pp. 67–78, Feb. 2009.
- [29] R. Ebrahimi, S. Okazawa, R. Rohling, and S. E. Salcudean, "Hand-held steerable needle device," in *Proc. Med. Image Comput. Comput.-Assisted Intervention*, 2003, pp. 223–230.
- [30] S. Okazawa, R. Ebrahimi, J. Chuang, S. E. Salcudean, and R. Rohling, "Hand-held steerable needle device," *IEEE/ASME Trans. Mechatronics*, vol. 10, no. 3, pp. 285–296, Jun. 2005.
- [31] D. C. Rucker, B. A. Jones, and R. J. Webster, III, "A geometrically exact model for externally loaded concentric tube continuum robots," *IEEE Trans. Robot.*, vol. 26, no. 5, pp. 769–780, Oct. 2010.
- [32] P. Sears and P. Dupont, "A steerable needle technology using curved concentric tubes," in *Proc. IEEE/RSJ Int. Conf. Intell. Robot. Syst.*, 2006, pp. 2850–2856.
- [33] S. E. Song, J. Tokuda, K. Tuncali, C. M. Tempny, E. Zhang, and N. Hata, "Development and preliminary evaluation of a motorized needle guide

- template for MRI-guided targeted prostate biopsy," *IEEE Trans. Biomed. Eng.*, vol. 60, no. 11, pp. 3019–3027, Nov. 2013.
- [34] A. Majewicz, T. Wedlick, K. B. Reed, and A. M. Okamura, "Evaluation of robotic needle steering in *ex vivo* tissue," in *Proc. IEEE Int. Conf. Robot. Autom.*, 2010, pp. 2068–2073.
- [35] T. Wedlick and A. M. Okamura, "Characterization of pre-curved needles for steering in tissue," in *Proc. IEEE Int. Conf. Eng. Med. Biol. Soc.*, 2009, pp. 1200–1203.
- [36] W. S. Ahn, J. H. Bahk, Y. J. Lim, and Y. C. Kim, "The effects of needle type, gauge, and tip bend on spinal needle deflection," *Anesth. Analg.*, vol. 82, no. 2, pp. 297–301, 1996.
- [37] R. J. Webster, III, A. M. Okamura, and N. J. Cowan, "Toward active cannulas: Miniature snake-like surgical robots," in *Proc. IEEE/RSJ Int. Conf. Intell. Robot. Syst.*, Oct. 2006, pp. 2857–2863.
- [38] J. Lock, G. Lain, M. Mahvash, and P. E. Dupont, "Quasistatic modeling of concentric tube robots with external loads," in *Proc. IEEE/RSJ Int. Conf. Intell. Robot. Syst.*, 2010, pp. 2325–2332.
- [39] P. Dupont, J. Lock, B. Itkowitz, and E. Butler, "Design and control of concentric tube robots," *IEEE Trans. Robot.*, vol. 26, no. 2, pp. 209–225, Apr. 2010.
- [40] J. Lock and P. Dupont, "Friction modeling in concentric tube robots," in *Proc. IEEE Int. Conf. Robot. Autom.*, May 2011, pp. 1139–1146.
- [41] P. Sears and P. E. Dupont, "Inverse kinematics of concentric tube steerable needles," in *Proc. IEEE Int. Conf. Robot. Autom.*, 2007, pp. 1887–1892.
- [42] D. C. Rucker and R. J. Webster, III, "Mechanics-based modeling of bending and torsion in active cannulas," in *Proc. IEEE RAS/EMBS Int. Conf. Biomed. Robot. Biomechanics*, Oct. 2008, pp. 704–709.
- [43] E. Lobaton, J. Zhang, S. Patil, and R. Alterovitz, "Planning curvature-constrained paths to multiple goals using circle sampling," in *Proc. IEEE Int. Conf. Robot. Autom.*, May 2011, pp. 1463–1469.
- [44] E. M. Boctor, P. Stolka, C. Clarke, D. C. Rucker, J. M. Croom, E. C. Burdette, and R. J. Webster, III, "Precisely shaped acoustic ablation of tumors utilizing steerable needle and 3D ultrasound image guidance," in *Proc. SPIE Med. Imag.*, 2010, pp. 76252N-1–76252N-10.
- [45] E. C. Burdette, D. C. Rucker, P. Prakash, C. J. Diederich, J. M. Croom, C. Clarke, P. J. Stolka, T. Juang, E. M. Boctor, and R. J. Webster, III, "The ACUSITT ultrasonic ablator: The first steerable needle with an integrated interventional tool," in *Proc. SPIE Med. Imag.*, 2010, pp. 76290V-1–76290V-10.
- [46] P. J. Swaney, J. Burgner, T. S. Pfeiffer, D. C. Rucker, H. B. Gilbert, J. E. Ondrake, A. L. Simpson, E. C. Burdette, M. I. Miga, and R. J. Webster, III, "Tracked 3D ultrasound targeting with an active cannula," in *Proc. SPIE Med. Imag.*, 2012, p. 83160R.
- [47] J. Burgner, P. J. Swaney, T. L. Bruns, M. S. Clark, D. C. Rucker, E. C. Burdette, and R. J. Webster, III, "An autoclavable steerable cannula manual deployment device: Design and accuracy analysis," *ASME J. Med. Devices*, vol. 6, no. 4, p. 041007, 2012.
- [48] H. Su, D. Cardona, W. Shang, G. A. Cole, C. Rucker, R. Webster, III, and G. S. Fischer, "A MRI-guided concentric tube continuum robot with piezoelectric actuation: A feasibility study," in *Proc. IEEE Int. Conf. Robot. Autom.*, May 2012, pp. 1939–1945.
- [49] R. J. Webster, III, J. Memisevic, and A. M. Okamura, "Design considerations for robotic needle steering," in *Proc. IEEE Int. Conf. Robot. Autom.*, May 2005, pp. 3599–3605.
- [50] C. J. Walsh, J. Franklin, A. H. Slocum, and R. Gupta, "Material selection and force requirements for the use of precurved needles in distal tip manipulation mechanisms," in *Proc. Design Med. Dev. Conf.*, Apr. 2010, p. 027536.
- [51] E. Dehghan and S. E. Salcudean, "Needle insertion point and orientation optimization in non-linear tissue with application to brachytherapy," in *Proc. IEEE Int. Conf. Robot. Autom.*, Apr. 2007, pp. 2267–2272.
- [52] V. Lagerburg, M. A. Moerland, J. J. W. Lagendijk, and J. J. Battermann, "Measurement of prostate rotation during insertion of needles for brachytherapy," *Radiother. Oncol.*, vol. 77, pp. 318–323, Dec. 2005.
- [53] R. Alterovitz, K. Goldberg, J. Pouliot, R. Taschereau, and I. C. Hsu, "Sensorless planning for medical needle insertion procedures," in *Proc. IEEE/RSJ Int. Conf. Intell. Robot. Syst.*, Oct. 2003, pp. 3337–3343.
- [54] C. J. Walsh, A. H. Slocum, and R. Gupta, "Preliminary evaluation of robotic needle distal tip repositioning," in *Proc. SPIE Med. Imag.*, Feb. 2011, p. 790108.
- [55] C. Graves, A. Slocum, R. Gupta, and C. J. Walsh, "Towards a compact robotically steerable thermal ablation probe," in *Proc. IEEE Int. Conf. Robot. Autom.*, 2012, pp. 709–714.
- [56] C. J. Walsh, J. Franklin, A. H. Slocum, and R. Gupta, "Design of a robotic tool for percutaneous instrument distal tip repositioning," in *Proc. IEEE Int. Conf. Eng. Med. Biol. Soc.*, Aug. 2011, pp. 2097–2100.
- [57] P. C. Mozer, A. W. Partin, and D. Stoianovici, "Robotic image-guided needle interventions of the prostate," *Rev. Urol.*, vol. 11, pp. 7–15, Winter 2009.
- [58] P. Blumenfeld, N. Hata, S. DiMaio, K. Zou, S. Haker, G. Fichtinger, and C. M. Tempny, "Transperineal prostate biopsy under magnetic resonance image guidance: A needle placement accuracy study," *J. Magn. Reson. Imag.*, vol. 26, no. 3, pp. 688–694, 2007.
- [59] A. M. Okamura, C. Simone, and M. D. O'Leary, "Force modeling for needle insertion into soft tissue," *IEEE Trans. Biomed. Eng.*, vol. 51, no. 10, pp. 1707–1716, Oct. 2004.
- [60] T. K. Podder, D. P. Clark, J. Sherman, E. M. Messing, D. Fuller, D. J. Rubens, J. Strang, R. Brasacchio, L. Liao, W. S. Ng, and Y. Yuet, "In vivo motion and force measurement of surgical needle intervention during prostate brachytherapy," *J. Med. Phys.*, vol. 33, no. 8, pp. 2915–2922, 2006.
- [61] M. L. Fackler and J. A. Malinowski, "Ordinance gelatin for ballistic studies. Detrimental effect of excess heat used in gelatin preparation," *Amer. J. Forensic Med. Pathol.*, vol. 9, no. 3, pp. 218–219, Sep. 1988.
- [62] C. M. Able, M. Bright, and B. Frizzell, "Quality control of high-dose-rate brachytherapy: Treatment delivery analysis using statistical process control," *Int. J. Radiat. Oncol. Biol. Phys.*, vol. 85, no. 3, pp. 828–833, Mar. 2013.
- [63] A. Seitel, C. J. Walsh, N. C. Hanumara, J.-A. Shepard, A. H. Slocum, H.-P. Meinzer, R. Gupta, and L. Maier-Hein, "Development and evaluation of a new image-based user interface for robot-assisted needle placements with the Robopsy system," in *Proc. Med. Imag.: Visual., Imag.-Guid. Proced., Model.*, 2009, p. 72610X.
- [64] K. B. Reed, "Compensating for torsion windup in steerable needles," in *Proc. IEEE RAS/EMBS Int. Conf. Bio. Robot. Biomechanics*, Scottsdale, AZ, USA, Oct. 2008, pp. 936–941.
- [65] R. A. Lathrop, D. C. Rucker, and R. J. Webster, III, "Guidance of a steerable cannula robot in soft tissue using preoperative imaging and conoscopic surface contour sensing," in *Proc. IEEE Int. Conf. Robot. Autom.*, May 2010, pp. 5601–5606.
- [66] S. DiMaio, E. Samset, G. S. Fischer, I. Iordachita, G. Fichtinger, F. Jolesz, and C. Tempny, "Dynamic MRI scan plane control for passive tracking of instruments and devices," in *Proc. Med. Image Comput. Comput.-Assisted Intervention*, Nov. 2007, pp. 50–58.
- [67] J. Tokuda, G. S. Fischer, S. P. DiMaio, D. G. Gobbi, C. Csoma, P. W. Mewes, G. Fichtinger, C. M. Tempny, and N. Hata, "Integrated navigation and control software system for MRI-guided robotic prostate interventions," *J. Comput. Med. Imag. Graph.*, vol. 34, no. 1, pp. 3–8, 2010.
- [68] S. Pieper, B. Lorensen, W. Schroeder, and R. Kikinis, "The NA-MIC kit: ITK, VTK, pipelines, grids and 3D Slicer as an open platform for the medical image computing community," in *Proc. IEEE 3rd Int. Symp. Biomed. Imag.: From Nano Macro*, 2006, pp. 698–701.
- [69] J. Tokuda, G. S. Fischer, X. Papademetris, Z. Yaniv, L. Ibanez, P. Cheng, H. Liu, J. Blevins, J. Arata, A. Golby, T. Kapur, S. Pieper, E. C. Burdette, G. Fichtinger, C. M. Tempny, and N. Hata, "OpenIGTLink: An open network protocol for image-guided therapy environment," *Int. J. Med. Robot.*, vol. 5, no. 4, pp. 423–34, 2009.
- [70] J. C. Blasko, T. Mate, J. Sylvester, P. Grimm, and W. Cavanagh, "Brachytherapy for carcinoma of the prostate," *Semin. Radiat. Oncol.*, vol. 12, no. 1, pp. 81–94, 2002.
- [71] K. M. Pondman, J. J. Futterer, B. ten Haken, L. J. S. Kool, J. A. Witjes, T. Hambroek, J. Katarzyna, J. Macuracae, and J. O. Barentsz, "MR-guided biopsy of the prostate: An overview of techniques and a systematic review," *Eur. Urol.*, vol. 54, no. 3, pp. 517–527, 2008.
- [72] A. Rosset, L. Spadola, and O. Ratib, "OsiriX: An open-source software for navigating in multidimensional DICOM images," *J. Digit. Imag.*, vol. 17, no. 3, pp. 205–216, Sep. 2004.
- [73] K. Wallner, J. Blasko, and M. Dattoli, *Prostate Brachytherapy Made Complicated*, 2nd ed. Seattle, WA, USA: Smart Medicine, 2001.
- [74] A. L. Zietman, "Localized prostate cancer: Brachytherapy," *Curr. Treat. Options Oncol.*, vol. 3, pp. 429–36, Oct. 2002.
- [75] D. C. Rucker and R. J. Webster, III, "Statics and dynamics of continuum robots with general tendon routing and external loading," *IEEE Trans. Robot.*, vol. 27, no. 6, pp. 1033–1044, Jun. 2011.
- [76] C. Walsh, N. Hanumara, R. Gupta, J. Shepard, and A. Slocum, "Evaluation of a patient-mounted, remote needle guidance and insertion system for CT-guided, percutaneous lung biopsies," presented at the 2nd Frontiers Biomed. Dev. Conf., Irvine, CA, USA, Jun. 2007.



Meysam Torabi received the Diploma degree in mathematics and physics from the National Organization for Development of Exceptional Talents in Iran. He received the Bachelor's degree in control engineering from the University of Tehran, Tehran, Iran, in 2005 and the Master's degree in biomedical engineering from the Sharif University of Technology, Tehran, in 2008. He received the Master's degree in operations research from the University of California, Berkeley, Berkeley, CA, USA, in 2011, where he had a fellowship.

During 2011–2012, he followed his research interests at the Wyss Institute for Biologically Inspired Engineering, Harvard University, Cambridge, MA, USA. In 2013, he joined the Brigham and Women's Hospital, Harvard Medical School, Boston, MA. During the past six years while at Sharif University of Technology, University of California, Berkeley, and Harvard University, he has been focused on the development of safe computer-integrated robotic interventional procedures.



Conor James Walsh (M'12) received the B.A.I. and B.A. degrees in mechanical and manufacturing engineering from Trinity College Dublin, Dublin, Ireland, in 2003 and the M.S. and Ph.D. degrees in mechanical engineering from the Massachusetts Institute of Technology (MIT), Cambridge, MA, USA, in 2006 and 2010, respectively, with a minor in entrepreneurship from the Sloan School of Management, as well as a Certificate in Medical Science through the Harvard-MIT Division of Health Sciences and Technology.

During his time at MIT, he received the Whitaker Health Sciences Fund Fellowship, as well as numerous other design, entrepreneurship, and mentoring awards. He is currently an Assistant Professor with the Harvard School of Engineering and Applied Sciences and a Core Faculty Member with the Wyss Institute for Biologically Inspired Engineering, Harvard University, Cambridge. His research focus is on research efforts at the intersection of science, engineering, and medicine with a focus on developing smart medical devices for diagnostic, therapeutic, and assistive applications.



Rajiv Gupta received the B.E. (Hons.) and M.Sc. (Hons.) degrees in electrical engineering and physics from the Birla Institute of Technology and Science, Pilani, India, and the M.S. and Ph.D. degrees in computer science from the State University of New York, Stony Brook, NY, USA, and the M.D. degree from Cornell University, Ithaca, NY, USA, in 2001.

He worked for 12 years in academia (University of Southern California, Los Angeles, CA, USA) and industry (GE Global Research Center, Niskayuna, NY, USA). He completed his residency and fellowships in cardiac and neuro radiology at the Massachusetts General Hospital (MGH)/Harvard Medical School. He is currently an Assistant Radiologist with MGH and the Director of the Ultra-high Resolution Volume CT Lab.